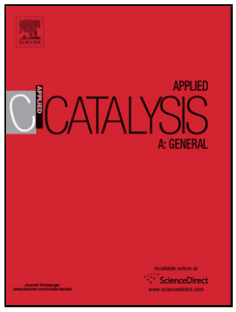

Title: Nickel Nanoparticles Supported on Silica for the Partial Oxidation of Isooctane

Authors: Qusay Bkour, Oscar G. Marin-Flores, Trent R. Graham, Parissa Ziaei, Steven R. Saunders, M.Grant Norton, Su Ha

PII: S0926-860X(17)30385-X
DOI: http://dx.doi.org/doi:10.1016/j.apcata.2017.08.015
Reference: APCATA 16370

To appear in: *Applied Catalysis A: General*

Received date: 31-5-2017
Revised date: 27-7-2017
Accepted date: 10-8-2017

Please cite this article as: Qusay Bkour, Oscar G.Marin-Flores, Trent R.Graham, Parissa Ziaei, Steven R.Saunders, M.Grant Norton, Su Ha, Nickel Nanoparticles Supported on Silica for the Partial Oxidation of Isooctane, Applied Catalysis A, Generalhttp://dx.doi.org/10.1016/j.apcata.2017.08.015

Nickel Nanoparticles Supported on Silica for the Partial Oxidation of Isooctane

Qusay Bkour[1], Oscar G. Marin-Flores[2] , Trent R. Graham[1], Parissa Ziaei[2] , Steven R. Saunders[1], M. Grant Norton[1,2*], Su Ha[1*]

[1]Voiland School of Chemical Engineering and Bioengineering, Washington State University, Pullman, WA, 99164, USA

[2]School of Mechanical and Materials Engineering, Washington State University, Pullman, WA, 99164, USA

Corresponding Authors:

suha@wsu.edu (S. Ha) and mg_norton@wsu.edu (M.G. Norton)

GRAPHICAL ABSTRACT

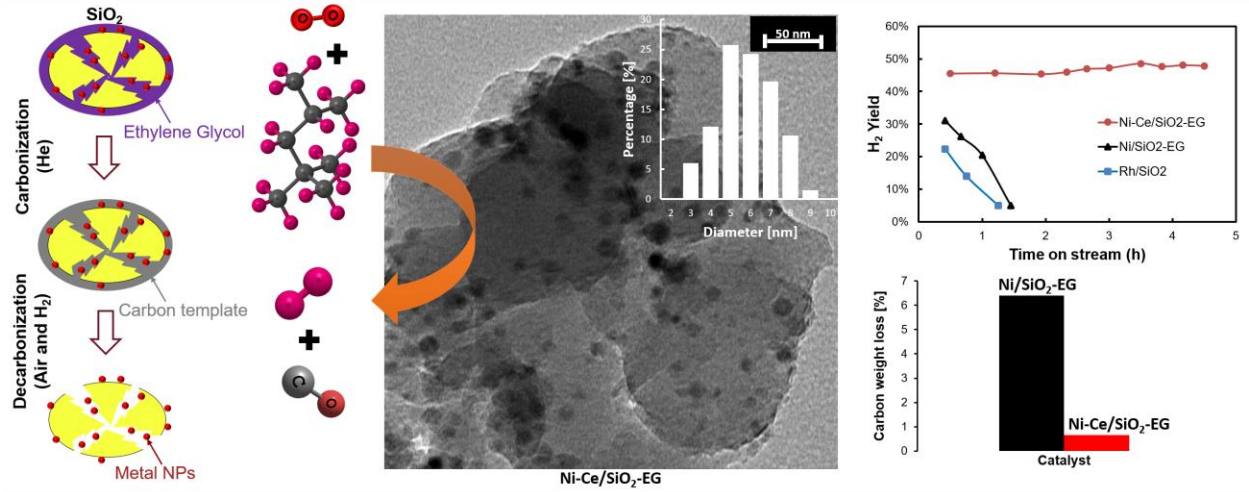

Highlights:

- Ni-Ce supported on SiO_2 was synthesized with ethylene glycol (EG) as solvent.
- Ni particle size prepared using EG and ceria promoter tend to be small.
- Ni/SiO_2-EG showed 97% conversion and 80% H_2 yield toward POX of isooctane.
- Ni-Ce/SiO_2-EG showed much improved coking resistance at high WHSV of 20.01 h^{-1}.
- Rh/SiO_2 showed severe deactivation at the same high WHSV of 20.01 h^{-1}.

A Ni-based nanoparticle catalyst was synthesized over a silica support via wet impregnation using either ethylene glycol or water. X-ray diffraction and transmission electron microscopy analysis showed that the particle size of the Ni catalyst prepared using ethylene glycol as the solvent tended to be smaller than that obtained when water was used. The resulting catalysts were tested for performance toward partial oxidation (POX) of isooctane at high weight hourly space velocities (WHSV). The results were compared with those from a Rh-based catalyst, which is commonly used for the same reaction. At a WHSV of 13.8 h^{-1}, a Ni/SiO_2 catalyst with an average Ni particle size of 6.8 nm exhibits higher catalytic activity and stability with an improved resistance to carbon formation than a Ni/SiO_2 catalyst with an average Ni particle size of 16.6 nm. The catalyst with the smaller Ni particles outperformed the supported Rh catalyst for the POX of isooctane. To further improve the Ni dispersion and enhance its ability to run at even higher WHSV with milliseconds of residence time, ceria was used as a promoter. The ceria-promoted Ni catalyst was also prepared by the wet impregnation method using ethylene glycol as the solvent. The addition of ceria corresponded with a reduction in the size of the Ni nanoparticles and improved Ni dispersion. Using the Ni-Ce/SiO_2 catalyst the

WHSV could be increased up to 20.01 h^{-1} while still maintaining its catalytic activity. The Ni/SiO_2 catalyst without the ceria promoter and the Rh catalyst showed severe deactivation due to the formation of surface carbon deposits.

Keywords: partial oxidation, isooctane, hydrogen, ethylene glycol, ceria

Introduction

Fuel cells can directly convert the chemical energy of gas and liquid fuels into electrical energy with a higher efficiency than conventional gas turbine engines (1,2). Fuel cells can operate using various types of conventional logistic fuels such as gasoline via fuel reforming processes, which enables the use of existing energy distribution networks. The production of hydrogen from heavy hydrocarbons is achieved by three main methods: steam reforming (SR), partial oxidation (POX), and auto-thermal reforming (ATR). Steam reforming is the most widely employed method in industry for hydrogen production from methane (3). The major drawback of SR for fuel cell applications is that it is a highly endothermic reaction, which leads to a slower startup and complex overall fuel cell system design. Furthermore, supplying water to the system requires extra energy for steam generation. POX and ATR are more attractive for practical fuel cell applications because POX reaction is mildly exothermic while ATR is energy neutral (4). Because POX generates heat it enables a faster startup and simpler system design, which makes it very suitable for distributed SOFC power generation and transportation (5,6).

Noble metals (e.g., Ru, Rh, Pd, Pt and Ir) are highly active and coking-resistant catalytic materials for hydrocarbon reforming (7,8). Nonetheless, their cost limits their application as catalysts. In contrast, nickel (Ni)-based catalysts have become promising alternatives to expensive noble-metals because of their availability, low cost, and high reforming activity (9,10). However, high operating temperatures, like those employed in reforming, promote unwanted side reactions and undesirable physical degradation that eventually lead to the deactivation of Ni catalysts. For example, Ni nanoparticles may aggregate via sintering to form larger metal clusters with a loss of a significant number of active sites. In addition, Ni can also deactivate via carbon formation resulting from undesirable hydrocarbon cracking reactions (11).

Catalyst supports such as YSZ (12), ZrO_2 (13), and GDC (14), and promoters such as cerium-zirconium (10) and boron (15) have been employed to improve the performance of Ni-based catalysts operating at high temperatures. However, most of these cited studies investigated supported Ni catalysts for reforming of simple hydrocarbons such as methane and not for reforming of heavy liquid hydrocarbons such as isooctane. Despite the introduction of supports and promoters, researchers still found significant amounts of coke deposition at high space velocities for these supported Ni catalysts toward the reforming of heavy liquid hydrocarbons. Corbo et al. (16) studied the performance of supported Ni-based catalysts for SR of various liquid fuels for only 5h at a WHSV of 20,000 h^{-1} and found that the catalysts deactivated because of carbon deposition. Dong et al. (17) investigated various types of supported transition metals including Ni for partial oxidation of isooctane and concluded that the hydrogen

concentration decreased significantly as the WHSV increased beyond 20,000 h^{-1} due to severe coking.

Small Ni particle sizes are able to limit carbon nucleation and subsequent growth, which decreases the rate of coking (11). There are several approaches that can be used to control particle size as well as to improve Ni metal dispersion. These include: strengthening metal-support interactions by employing suitable carriers and promoters (18–20), alloying with a metal of higher melting point (21), and physical confinement of nanoparticles on porous catalytic support (22). The last approach is believed to be the most effective. For example, many researchers have reported the catalytic activity of encapsulated Ni nanoparticles in mesoporous hosts and porous inorganic shell structures (23–26). Xie et al. (27) and Din et al. (28) prepared highly dispersed Ni nanoparticles immobilized within a mesoporous silica matrix using a polyol-assisted route as a removable carbon template for improving sintering and coking resistant. The encapsulated metal nanoparticle design demonstrated improved Ni dispersion, inhibited nanoparticle sintering, and hindered Ni migration from the mesoporous channels to the external surface.

Promoters are another key factor in the formulation of industrial catalysts as they can enhance catalytic performances in significant ways (29). For example, Ni catalysts are more stable, active and form less carbon during reforming processes when ceria is used as promoter (30,31). Zhenxing, et al. (32) studied the promoting effect of ceria in Ni/γ-Al_2O_3 for dry reforming of methane, and found that ceria can greatly enhance the activity.

In this work, Ni nanoparticles with different particle sizes supported by mesoporous SiO_2 were synthesized via a wet impregnation method using both aqueous and non-aqueous solvents, and tested for their catalytic activities toward the partial oxidation of isooctane at high WHSV. The Ni catalyst was promoted with ceria to further improve its dispersion over the support in order to increase its effective operating range. Moreover, in this research the fuel was vaporized when it was introduced through the top of the reactor without the need for an external vaporizer, which makes the system more compact. The results obtained demonstrate that Ni/SiO_2 catalyst samples prepared with the non-aqueous solvent have a smaller average particle size than those prepared using the aqueous solvent. Incorporation of ceria as the promoter appears to further decrease the average particle size and its dispersion over the support. As the average Ni particle size decreases, both the reforming activity and stability toward the POX of isooctane significantly increases with improved coking resistance.

Experimental

Catalyst Preparation Several silica (SiO_2)-supported Ni catalysts were prepared in this work using aqueous and non-aqueous wet impregnation of a Ni precursor on a commercial silica support. Based on the N_2 adsorption-desorption experiments, the commercial silica support (lot # G02M44, Alfa Aesar) possesses BET surface area, pore volume, and pore diameter range of 101.6 m^2/g, 0.25 cm^3/g, and 5-65 nm, respectively. In a typical preparation, 0.6 g of $Ni(NO_3)_2 \cdot 6H_2O$ (Alfa Aesar) with or without ceria precursor (0.1 g of cerium nitrate hexahydrate ($Ce(NO_3)_3 \cdot 6H_2O$), Alfa Aesar, 99.99%) was dissolved in 5 mL of Millipore water for aqueous impregnation or ethylene glycol

(anhydrous, Sigma Aldrich, 99.8%) for non-aqueous impregnation. Nickel and ceria contents were kept at 11 and 3 wt.%, respectively. The resulting solutions were mixed with 1 g of silica support (Alfa Aesar) and ultrasonicated before stirring at 70 °C for 1 h. The aqueous suspensions were dried overnight and then calcined at different temperatures (500-700 °C) in static air and reduced in hydrogen (H_2) at 700 °C for 3 h. With the non-aqueous solvent, the suspensions were first vacuum-dried for 3 h at 170 °C and then annealed in flowing helium (He) at 700 °C for 3 h to produce a carbon template by carbonization of ethylene glycol. The resulting carbon template was later removed during calcination in static air at 700 °C for 2 h. The samples were then reduced in H_2 at 700 °C for 3 h in a tube furnace. All reduced samples were cooled in flowing He to room temperature before removal from the tube furnace and were used without any further pretreatments prior to the reaction tests. For comparison purposes, a sample of 1% Rh/SiO_2 was prepared by dissolving an appropriate amount of rhodium chloride hydrate (Rh 38-40%, Aldrich) in 1:3 HNO_3 and HCl mixture, which was then impregnated on a SiO_2 support. The sample was calcined and reduced in H_2 for 3 h for each step at 700 °C and 500 °C, respectively, after drying for 24 h at 110 °C. The composition of the samples prepared in this study are summarized in **Table 1**.

Characterization: X-ray diffraction (XRD) patterns from Ni and Rh catalysts were obtained using a Rigaku Miniflex 600 diffractometer with Cu Kα radiation. Particle size measurements were made using transmission electron microscopy (TEM) with a FEI Technai G2 20 Twin. The morphology of the post-test catalysts was examined by scanning electron microscopy (SEM) using a FEI Quanta 200F SEM. Nitrogen adsorption-desorption isotherms were measured at -196 °C using a TriStar II 3020

automotive physisorption analyzer to obtain the BET surface area, total pore volume, and pore diameter for the SiO_2 support. Fourier transform infrared spectroscopy (FTIR) was used to characterize the presence of carbon after the carbonization step. FTIR spectra were obtained in the range of 1800-1300 cm^{-1} during 64 scans, with 2 cm^{-1} resolution, using attenuated total reflection (ATR) mode (ThermoScientific Nicolet IS10).

The amount of carbon deposited on the surface of the post-test catalysts was quantified using thermal gravimetric analysis (TGA) under air using TA instruments Q50. Samples were loaded in platinum crucibles and then heated with air from room temperature to 800 ^oC at a rate of 5 $^oC \cdot min^{-1}$.

Activity tests: The catalytic activity for the partial oxidation of isooctane was measured in a simplified quartz tube reaction system (see **Figure 1**). The catalyst samples were supported on a quartz wool plug inside a 7-mm quartz tube, which was heated by an electrical furnace. A K-type thermocouple was placed at the center of the catalyst bed to record and control its temperature. The temperature of the catalyst bed was maintained at the set point of 750 ^oC for our reforming tests. We also measured the inlet and outlet temperatures of the catalyst bed during the reforming reaction of isooctane at 750 °C and we did not observe any temperature changes. Isooctane and air were introduced through the top of the quartz tube, which allowed rapid vaporization of the liquid. A silicon carbide bed was placed between the inlet and the catalyst bed to enhance the mixing of reactants. A calibrated syringe pump and a mass flow controller were used to control the flow rates of liquid fuel and air, respectively. The exit stream was cooled to 5 ^oC to separate water, non-reacted fuel, and other possible condensable compounds. The dry gaseous product

thus obtained was analyzed using a gas chromatograph equipped with two packed columns (Molecular Sieve 13X and HayeSep D) and a TCD detector.

The amounts of fuel and air were adjusted to obtain different space velocities at a constant oxygen-to-carbon molar ratio (O_2/C) of 0.5. The catalyst performance was evaluated in terms of H_2 yield, CO yield, and carbon conversion, which were calculated as shown below:

$$H_2 \text{ Yield} = \frac{2\times\text{moles of } H_2 \text{ produced}}{18\times\text{moles of isooctane fed}}\times 100\% \quad (1)$$

$$\text{CO Yield} = \frac{\text{moles of CO produced}}{8\times\text{moles of isooctane fed}}\times 100\% \quad (2)$$

$$\text{Carbon Conversion} = \frac{\text{moles of } (CO+CO_2+CH_4) \text{ produced}}{8\times\text{moles of isooctane fed}}\times 100\% \quad (3)$$

Prior to testing, the catalysts were subjected to *in-situ* activation. To do so, the samples were reduced by a H_2/N_2 mixture at 750 ^oC for 30 min.

Thermodynamic considerations

The partial oxidation of isooctane is believed to be the result of a multitude of reactions including total oxidation, steam reforming, dry reforming, and water-gas shift, which all occur to varying degrees. Secondary reactions may also take place between reactants and products, for instance, methanation and carbon deposition through the Boudouard reaction (**Table 2**). These reactions occur on the surface of the catalyst as well as in the gas phase (33,34). Equilibrium concentrations were calculated using Gibbs free energy minimization and the results are reported in **Figure 2**. Under the operating

conditions used in these calculations, the formation of C2 compounds is almost negligible and the carbon conversion of isooctane is ~100%. **Figure 2 (A)** shows the effect of the O_2/C ratio on the composition of the product stream at 750 ^oC. For values of O_2/C between 0.5 and 0.7 (the shaded area of **Figure 2(A)**), the carbon formation can be minimized with high concentrations of H_2 and CO and low amounts of CO_2 and H_2O. If O_2/C values are higher than 0.7, the carbon formation can be completely suppressed. However, considerable amounts of H_2O and CO_2 are produced at the expense of syngas as complete combustion becomes dominant. **Figure 2 (B)** shows the effect of the reaction temperature at O_2/C of 0.5. Temperatures higher than 750 ^oC favor the production of H_2 and CO over CO_2 and H_2O with a minimum amount of the carbon formation. Based on this thermodynamic result, the catalytic activity tests were performed at 750 ^oC and O_2/C ratio of 0.5 for our studies.

Results and discussion

The XRD patterns of the as-prepared samples are shown in **Figure 3**. The nickel oxide (NiO) phase was entirely transformed into metallic nickel (Ni) after the reduction step, as deduced from the absence of peaks associated to the NiO phase and the appearance of the metallic Ni planes (111) and (200) at 44.7° and 52.0°, respectively (JCPDS No. 04-0850). The Scherrer equation was used to calculate the average crystallite size of the metallic Ni phase and the values are reported in **Table 3**. As seen, the average crystallite sizes for the samples prepared using aqueous impregnation were larger than those using non-aqueous impregnation. These results agree with previous reports (28), which indicate

that the Ni crystallite size of catalysts prepared using ethylene glycol tend to be smaller than those prepared with water.

In aqueous impregnations, water is completely evaporated during drying. In the calcination process, nickel nitrate decomposes to NiO, which easily agglomerates to form larger particles (35). If the solvent is ethylene glycol, the carbon template is formed from the carbonization of ethylene glycol by heating it under He conditions at 700 °C. Nickel nitrate decomposes to NiO under the confinement of the carbon template during the air calcination process, resulting in well-dispersed and small NiO nanoparticles. The carbon template would be removed during calcination. However, we believe that the time of air exposure without the carbon template was sufficiently short to prevent the severe aggregation of NiO nanoparticles. The presence of these small NiO nanoparticles eventually leads to the formation of highly dispersed Ni nanoparticles following the reduction process. Many researchers also studied the carbonization of ethylene glycol and the formation of a carbon template. Miao et al. (36) used ethylene glycol as a carbon source to fill an aluminum oxide template and they found that high temperature carbonization for 30 min resulted in the formation of carbon nanotubes. Xie et al. (27) reported that the nickel nitrate can coordinate with ethylene glycol and enters the silica channels by the capillary force. During the inert gas heat treatment, ethylene glycol then decomposes to carbon and forms the carbon template that hinders NiO nanoparticles from sintering by preventing the migration of nanoparticles from the internal surface of silica channels to the outside. TEM analysis performed after the pyrolysis step showed that the mesoporous channels of SiO_2 were filled with the carbon templates under the inert gas heat treatment and NiO nanoparticles were immobilized under the carbon

template without sintering during the calcination step. They also collected Raman spectra and found distinct peaks that were assigned to carbonaceous matrix after the carbonization of ethylene glycol. After calcination, the peaks vanished, indicating the removal of the carbon template. In this work, the presence of carbon template before the calcination process was determined using FTIR (**Figure S1**) for NS-EG sample. A distinct peak at 1580 cm^{-1} before exposure to air was detected, which is assigned to C=C stretching, indicating the presence of a carbonaceous matrix from the carbonization of ethylene glycol. After being exposed to air during the calcination process at 700 °C, the peak almost completely disappeared indicating the removal of the carbon template (37).

Figure 4 (A, B, and C) shows TEM images combined with particle size distributions for all the Ni-containing samples. As seen, the NS-EG exhibits a particle size distribution with a peak at ~8 nm and average particle size of 6.8 nm, while the samples that were prepared using water as a solvent display larger average particle sizes of 16.6 and 12.7 nm for NS-W700 and NS-W500, respectively. **Table 3** compares the TEM results with those obtained using XRD. Standard deviations for TEM particle size measurements is also provided in Table 3.

Beside the confinement effect of the carbon template for the ethylene glycol solvent, there could be other possible solvent effects improving Ni dispersion and catalytic properties such as chemical modification of the silica surface and improvement of the reducibility of supported metals. For example, Zhang et al (38) used different solvents (acetic acid or ethanol) to modify the surface properties of silica to improve the reducibility and dispersion of supported cobalt, which resulted in excellent stability for the Fischer-Tropsch synthesis reaction. Furthermore, the physical and chemical properties of the

metal species on the silica surface can be also strongly affected by the pH of the solvent as the charge on the silica surface changes as a function of solvent pH. At lower pH values (pH <2), the silica surface is positively charged and, consequently, metal ions with a positive charge are poorly dispersed (39). On the other hand, the surface of silica is negatively charged at higher pH values than 2, leading to greater dispersion of metal ions and formation of smaller supported metal nanoparticles (38,40,41). Miao et al. (42) reported that Ni/SBA-15 prepared from ethanol solution would promote the fixation of the precursor onto the silica support and increase Ni dispersion. As a result, the activity of catalysts for CO methanation was improved. They found that the effect of impregnation solvents could be related to the solubility of nickel nitrate and the polarities of solvents. The decreased polarity of the ethanol solvent caused an increase in the interaction between the metal complex and silanol group on the silica surface, promoting the fixation of the precursor onto the support and increased nickel dispersion (43). Lucredio et al. (44) prepared cobalt catalysts on SiO_2 and Al_2O_3 supports by impregnation using methanol. They found that a methanol solution led to smaller crystallites compared to that obtained with an aqueous solution because the methanol hydroxyl groups have a strong interaction with the silica surface. In addition to the carbon template effect, these other possible solvent effects could play an important role for improving the Ni dispersion for the Ni/SiO_2 catalyst synthesized using ethylene glycol.

A series of isooctane partial oxidation activity tests for NS-EG, NS-W500, and NS-W700 (with particle sizes of 6.8, 12.7, and 16.6 nm) were performed at different WHSVs to determine the maximum WHSV value that each catalyst sample can process without severe coking. The reforming tests were performed at fixed temperature and O_2/C of 750

°C and of 0.5, respectively. The fuel flow rate was changed to obtain different WHSV values. The maximum WHSV was determined by catalyst deactivation due to the severe carbon formation, at which point there was no syngas in the effluent stream and the performance drops significantly (i.e., the conversion drops down to that of the blank run, which is about 30%). The results are shown in **Figure 5**. As the Ni particle size decreases, there are more active sites available for processing higher amount of fuel per unit time. Thus, higher dispersion and smaller Ni particles lead to higher maximum WHSV values as shown in **Figure 5**. If the WHSV is too high (i.e., beyond the maximum WHSV value), then there would be insufficient surface area available for the catalyst to process all of the incoming fuel. In other words, there would be a large amount of fuel and their fragments that would not interact with the catalyst. Thus, the chance of coke formation increases.

A second set of fuel reforming experiments was carried out under the fixed high fuel flow rate (WHSV of 13.8 h^{-1}) for 2 h in order to compare the degree of coke formation in each sample. TGA was used to obtain quantitative information regarding the deposited carbon on the catalyst surface. According to **Figure 6**, the TGA profiles initially experienced an increase trend starting at 250 ^{o}C, which is derived from the oxidation of metallic Ni (45). The weight losses after 400 ^{o}C are caused by the oxidation of carbon (46,47). The NS-W700 sample with average particle size of 16.6 nm shows the highest weight loss, which is attributed to the presence of the largest amount of coke formation (~17 wt.%). On the other hand, the NS-EG sample with average particle size of 6.8 nm exhibited superior activity at this high space velocity with less than 3.3 wt.% coke formation. It has been shown that the coke depositions on Ni catalysts may be present in different morphologies

such as amorphous, filamentous, or graphitic carbon (48). Filamentous carbon over Ni particles, which originates from the polymerization reaction of hydrocarbons (49), is generally oxidized at temperatures between 300 and 530 ^{o}C (50). More stable graphitized carbon is expected to be oxidized at temperatures higher than 530 ^{o}C (51). The oxidation weight loss curves as a function of temperature measured by TGA are shown in **Figure S2** (black line) together with the corresponding derivative curves of the weight loss to temperature (red line). A major derivative peak is observed in the temperature range of 450 – 680 ^{o}C for all samples. These peaks are ascribed to the oxidation of both filamentous carbon as well as graphitic carbon. The peaks with large particle sizes (16.6 and 12.7 nm) were shifted to higher temperatures, due to higher degree of graphitization. The TGA results show that the sample with the smaller particle size exhibits higher resistance to carbon formation. The cleavage of C-H bonds and polymerization of C species on the Ni surface are dependent on the variation of Ni particle size and dispersion (35,52). It has been reported in the literature that carbon formation is not able to proceed when the crystals are below a critical ensemble size (53). carbon can grow only on Ni crystals larger than this critical ensemble size at certain temperatures and fuel flow rates (54). Kim et al. (55) observed that the formation of carbon proceeded over Ni particles > 7 nm. Others consider the critical ensemble size of Ni particles to be 10 nm (56,57). Our results agree with those reported in the literature, which shows that smaller and well dispersed Ni crystals have higher resistance to carbon formation (58). Thus, the NS-EG catalyst that possesses the smallest particle size shows the best reforming performance toward POX of isooctane.

It is also important to maintain the high dispersion and to prevent the Ni nanoparticles from aggregation during the reforming reaction at high temperatures in order to achieve long-term stability. TEM images and particle size distribution of spent NS-EG (**Figure S3 A**) showed that its average particle size only increases from 6.8 nm to 8.3 nm after the reforming reaction, while maintaining good Ni nanoparticle dispersion. TEM images indicates no carbon deposition. On the other hand, NS-W700 and NS-W500 spent samples (**Figure S4**) showed a significant increase of their average particle size from 16.6 to 32 nm and from 12.7 to 25 nm, respectively. Corresponding TEM images show a high degree of carbon deposition with a formation of carbon filaments.

To further investigate the stability of the NS-EG catalyst, activity tests were conducted over 12 h at 750 ^{o}C and 1 atm, with a WHSV of 13.8 h^{-1}, a residence time (RT) of 35 ms, and O_2/C ratio of 0.5. For our current study, a Rh/SiO_2 catalyst with 1% Rh loading (with particle size of 2.8 nm (**Figure S5 A**)) was chosen as a reference because it has been extensively used as an active catalyst for complex fuel reforming applications. The blank run shows a performance of 32 % conversion, 22% CO yield, 5% H_2 yield and 3 sccm of H_2 production. As seen in **Figure 7**, NS-EG catalyst showed stability for 12 h under these conditions and produced a conversion of 97%, H_2 yield of 80%, CO yield of 85%, CO_2 yield of 6% and syngas production of 70-75 sccm, while the Rh catalyst showed a much lower performance (conversion of 65%, H_2 yield of 20%, CO yield of 50%, CO_2 yield of 9% and syngas production of 30 sccm). Rh/SiO_2 spent sample (**Figure S5 B**) showed a particle size of 5.4 nm, which is even smaller than that of the NS-EG sample. Since the smaller particle size generally leads to both higher surface area and improved coking

resistance, our results shown in **Figure 7** suggest that our NS-EG catalyst might possess higher intrinsic catalytic properties than that of the Rh/SiO_2 catalyst.

Effect of ceria addition on the catalytic performance: The NS-EG sample with the particle size of 6.8 nm has a good catalytic activity and stability at the maximum WHSV of 13.8 h^{-1} (**Figure 5**). For practical applications in SOFC systems, it is crucial to design a catalyst that can handle the high WHSV with milliseconds of residence time and without deactivation due to the carbon formation. Ceria (Ce) is a good promoter for hydrocarbon reforming on Ni-based catalysts (30,31), and can promote carbon removal, enhance the dispersion of Ni on the support, and enhance catalytic activity (59,60). Ni-Ce supported on SiO_2 was synthesized using the wet impregnation method with ethylene glycol as solvent. The XRD diffractogram (**Figure 3 (D)**) shows that the incorporation of Ce as the promoter appears to further decrease the average crystallite size of Ni, which suggests that the presence of Ce may increase the metal dispersion. The absence of any of Ce diffraction peaks for the Ni catalysts suggests the high dispersion of promoter. **Figure 4 (D)** shows that NCS-EG sample with a narrow distribution of Ni particle sizes with a peak at ~5 nm (**Table 3**).

To investigate the effect of the Ce addition on the catalytic performance, POX of isooctane was carried out under harsher conditions than those used to obtain the data in Figure 7 (WHSV=20.01, and residence time =23 ms) for 4 h or until excessive carbon formation led to reactor plugging. As observed in **Figure 8**, NS-EG and RS-AR catalysts showed a rapid drop in performance under this high WHSV value caused by reactor plugging with an excessive amount of carbon deposition. On the other hand, the performance of the

NCS-EG catalyst exhibited reasonable stability with carbon conversion and syngas production of 78% and 70 sccm, respectively.

Effect of Ce addition on carbon formation: Carbon formation is a major problem in liquid hydrocarbon reforming since it can cause a loss of activity when it blocks the active sites. The coke can be formed by the Boudouard reaction (Equation 1) or by hydrocarbon cracking (Equation 2) (61).

$$2CO \rightleftarrows CO_2 + C \qquad \text{(Equation 1)}$$

$$C_nH_{2m} \rightleftarrows nC + mH_2 \qquad \text{(Equation 2)}$$

The quantification of the total carbon formation on NS-EG and NCS-EG samples was obtained by thermogravimetric analyses (TGA) after the activity tests at accelerated conditions at a WHSV of 20.01 h^{-1} (**Figure 9**). Weight losses before 130 ^oC were excluded as they are caused by the loss of adsorbed water. The weight gain observed for both samples is caused by the oxidation of Ni metal to NiO. The subsequent weight losses are caused by the removal of carbonaceous species (62). The weight loss of NS-EG (6.40 %) was found to be much higher than that of NCS-EG (0.66%) suggesting that the addition of the Ce promoter significantly enhances the coking tolerance of Ni catalysts.

In **Figure S6**, we differentiated the weight loss data of TGA shown in **Figure 9** as a function of temperature. As indicated in **Figure S6**, the derivative peak with NS-EG spent catalyst was shifted to higher temperature compared to that of the NCS-EG spent catalyst due to higher degree of graphitization of the coke deposit. These TGA results show that the NCS-EG sample with the smaller particle size exhibits higher resistance to carbon formation compared to that of NS-EG sample with the larger particle size. **Figure 10**

shows SEM images of the post-test catalysts. As seen, carbon whiskers are clearly observed on the spent NS-EG catalyst. While the spent NCS-EG shows negligible carbon formation. Particle size distribution and dispersion of spent NCS-EG (**Figure S3 A**) showed a good dispersion after the reforming reaction with average particle size of 5.8 nm and without any indication of carbon deposition. In summary, the results of our study show that (1) utilizing the ethylene glycol solvent for the supported Ni nanoparticle synthesis and (2) the addition of Ce to the Ni catalyst result in a $NiCe/SiO_2$ catalyst with a reduced Ni particle size and an increased Ni dispersion on the support, lead to superior performance for POX of isooctane, the improved coking resistance, and the increased operating WHSV window.

These results agree with other reports that studied the effect of Ni dispersion and particle size to suppress carbon deposition during reforming of heavy hydrocarbons, such as isooctane and dodecane. Some of these reports added different promoters and/or non-noble metals to prevent Ni growth in order to mitigate carbon formation and strengthen the interaction between Ni nanoparticles and the support (63,64). Bkour et al (10) found that the presence of Mo maintains the small size of the Ni particles and lowers the tendency for Ni nanoparticle growth, which hence prevent surface coking during POX of isooctane at the high WHSVs. Tin (Sn) is another element used to improve the stability during liquid hydrocarbon reforming. Nikolla et al (65) demonstrated that the Ni/Sn bimetallic system has much better carbon tolerance than monometallic Ni during steam reforming of isooctane. They found that the presence of Sn can decrease the ensemble size of low-coordinated Ni atoms that bind carbon strongly (66,67). Other studies have attempted to improve the catalytic activity of liquid fuel reforming by noble metal doping.

Gue at al. (68) found that the addition of Ru keeps small and well dispersed metallic Ni particles improving their catalytic activity for steam reforming of kerosene. Most of these studies used low space velocities and/or excess amounts of steam, which are not practical operating conditions for fuel cell systems. Ibrahim et al. (69) studied the effects of reaction operation conditions on the performance of the Ni/Al_2O_3 catalysts for the partial oxidation of isooctane. They confirmed that the high nickel dispersion helps to enhance the catalyst performance. Furthermore, the confinement of Ni nanoparticles to porous supports for improving Ni dispersion and suppressing aggregation is an effective strategy to operate catalytic reforming at high fuel space velocities (70). Xiao et al (71) found that alloying of Ni-Co along with the addition of Ce promoter and confinement of Ni nanoparticles are needed to improve Ni catalytic performance during steam reforming of *n*-dodecane at the high space velocities.

Conclusion

Controlling the metal particle size and improving its dispersion over the support can be achieved by utilizing the appropriate impregnation solvent and promoter. In this study, Ni-based catalysts were synthesized via the wet impregnation method using either water or ethylene glycol as solvents and were analyzed for the isooctane POX reaction at high space velocities. Based on TEM and XRD analysis, Ni nanoparticles supported on SiO_2 (i.e., Ni/SiO_2 catalyst) synthesized using ethylene glycol show the smaller and more highly dispersed Ni nanoparticles than Ni/SiO_2 catalyst synthesized using water. When ethylene glycol is used it creates a carbon template that confines the Ni metal nanoparticles and prevents agglomeration, which leads to improved Ni metal dispersion over SiO_2 support.

POX of isooctane was carried out at 750 °C, O_2/C ratio of 0.5, and WHSV of 13.8 h^{-1}. Ni/SiO_2 catalyst prepared in ethylene glycol with the average Ni size of 6.8 nm exhibit higher catalytic activity and stability with an improved resistance to carbon formation compared with Ni/SiO_2 catalyst prepared in aqueous solution with the average Ni size greater than 12 nm. The Ni/SiO_2 catalyst prepared with ethylene glycol provides isooctane conversion of 95%, CO and H_2 yields of 84% and 81%, respectively, and syngas production of 73 sccm for 12 h, which outperforms a supported Rh/SiO_2 catalyst at the same operating conditions. To further improve the Ni dispersion and enhance its capability to run at even higher WHSV with milliseconds of residence time, a Ce promoter was introduced. The Ni-Ce/SiO_2 prepared in ethylene glycol has a smaller crystallite size and higher metal dispersion than in the absence of Ce. For both the Ni/SiO_2 catalyst without the Ce promoter and the Rh/SiO_2 catalyst, our results show that severe deactivation occurs due to coking during the reforming reactions of liquid hydrocarbons at the accelerated coking condition (WHSV of 20.01 h^{-1}). On the other hand, under this very harsh operating condition, Ni-Ce/SiO_2 catalyst exhibits high catalytic activity with improved coking resistance.

Acknowledgements

This work was financially supported by the Office of Naval Research (Grant No. N00014-15-1-2416). We thank the Franceschi Microscopy and Imaging Center at Washington State University for use of their facilities. We also would like to show our gratitude to Jake Gray at Washington State University for taking the TEM images.

References

1. Hackett GA, Gerdes K, Song X, Chen Y, Shutthanandan V, Engelhard M, et al. Performance of solid oxide fuel cells operated with coal syngas provided directly from a gasification process. J Power Sources. 2012;214:142–52.

2. Feroldi D, Serra M, Riera J. Energy Management Strategies based on efficiency map for Fuel Cell Hybrid Vehicles. J Power Sources. 2009;190(2):387–401.

3. Kalamaras CM, Efstathiou a. M. Hydrogen Production Technologies: Current State and Future Developments. Conf Pap Energy. 2013;2013:9.

4. Pengpanich S, Meeyoo V, Rirksomboon T, Schwank J. iso-Octane partial oxidation over Ni-Sn/$Ce_{0.75}Zr_{0.25}O_2$ catalysts. Catal Today. 2008;136(3–4):214–21.

5. Cheekatamarla PK, Finnerty CM. Synthesis gas production via catalytic partial oxidation reforming of liquid fuels. Int J Hydrogen Energy. 2008;33(19):5012–9.

6. Schwank, Johannes W. and ART. Catalytic reforming of liquid hydrocarbons for on-board solid oxide fuel cell auxiliary power units. In: Catalysis 22. 2010. p. 56–93.

7. Yu J, Zhang Z, Dallmann F, Zhang J, Miao D, Xu H, et al. Facile synthesis of highly active Rh/Al_2O_3 steam reforming catalysts with preformed support by flame spray pyrolysis. Appl Catal B Environ. 2016;198:171–9.

8. Roy PS, Park CS, Raju ASK, Kim K. Steam-biogas reforming over a metal-foam-coated (Pd-Rh)/($CeZrO_2$-Al_2O_3) catalyst compared with pellet type alumina-supported Ru and Ni catalysts. J CO_2 Util. 2015;12:12–20.

9. Garcia-Dieguez M, Pieta IS, Herrera MC, Larrubia MA, Alemany LJ. Nanostructured Pt- and Ni-based catalysts for CO_2-reforming of methane. Sect Title Foss Fuels, Deriv Relat Prod. 2010;270(1):136–45.

10. Bkour Q, Zhao K, Scudiero L, Yoon CW, Marin-Flores OG, Norton MG HS. Synthesis and performance of ceria-zirconia supported Ni-Mo nanoparticles for

partial oxidation of isooctane. Appl Catal B Environ. 2017;212:97–105.

11. Wu J, Peng Z, Bell AT. Effects of composition and metal particle size on ethane dehydrogenation over Pt_xSn_{100-x}/Mg(Al)O (70<x<100). J Catal. 2014;311:161–8.

12. Wang Y, Yoshiba F, Kawase M, Watanabe T. Performance and effective kinetic models of methane steam reforming over Ni/YSZ anode of planar SOFC. Int J Hydrogen Energy. 2009;34(9):3885–93.

13. Nguyen LQ, Abella LC, Gallardo SM, Hinode H. Effect of nickel loading on the activity of Ni/ZrO_2 for methane steam reforming at low temperature. React Kinet Catal Lett. 2008;93(2):227–32.

14. HUANG T, HUANG M. Effect of Ni content on hydrogen production via steam reforming of methane over Ni/GDC catalysts. Chem Eng J. 2008;145(1):149–53.

15. Xu J, Chen L, Tan KF, Borgna A, Saeys M. Effect of boron on the stability of Ni catalysts during steam methane reforming. J Catal. 2009;261(2):158–65.

16. Corbo P, Migliardini F. Natural gas and biofuel as feedstock for hydrogen production on Ni catalysts. J Nat Gas Chem. 2009;18(1):9–14.

17. Moon DJ, Ryu JW, Lee SD, Lee BG, Ahn BS. Ni-based catalyst for partial oxidation reforming of iso-octane. Appl Catal A Gen. 2004;272(1–2):53–60.

18. Foo SY, Cheng CK, Nguyen T-H, Kennedy EM, Dlugogorski BZ, Adesina AA. Carbon deposition and gasification kinetics of used lanthanide-promoted Co-Ni/Al2O3 catalysts from CH_4 dry reforming. Catal Commun. 2012;26:183–8.

19. Wang S, Lu GQM. CO_2 reforming of methane on Ni catalysts: Effects of the support phase and preparation technique. Appl Catal B Environ. 1998;16(3):269–77.

20. Wang SB, Lu GQM. CO_2 reforming of methane on Ni catalysts: Effects of the support phase and preparation technique. Appl Catal B-Environmental. 1998;16(3):269–77.

21. Huang T, Huang W, Huang J, Ji P. Methane reforming reaction with carbon

dioxide over SBA-15 supported Ni-Mo bimetallic catalysts. Fuel Process Technol. 2011;92(10):1868–75.

22. Zhao X, Li H, Zhang J, Shi L, Zhang D. Design and synthesis of NiCe@m-SiO2 yolk-shell framework catalysts with improved coke- and sintering-resistance in dry reforming of methane. Int J Hydrogen Energy. 2016;41(4):2447–56.

23. Li Z, Kathiraser Y, Kawi S. Facile synthesis of high surface area yolk-shell Ni@Ni embedded SiO_2 via Ni phyllosilicate with enhanced performance for CO_2 reforming of CH_4. ChemCatChem. 2015;7(1):160–8.

24. Zheng X, Tan S, Dong L, Li S, Chen H. Silica-coated $LaNiO_3$ nanoparticles for non-thermal plasma assisted dry reforming of methane: Experimental and kinetic studies. Chem Eng J. 2015;265(0):147–56.

25. Li Z, Kathiraser Y, Ashok J, Oemar U, Kawi S. Simultaneous tuning porosity and basicity of nickel@nickel-magnesium phyllosilicate core-shell catalysts for CO_2 reforming of CH_4. Langmuir. 2014;30(48):14694–705.

26. Zhu QL, Li J, Xu Q. Immobilizing metal nanoparticles to metal-organic frameworks with size and location control for optimizing catalytic performance. J Am Chem Soc. 2013;135(28):10210–3.

27. Xie T, Shi L, Zhang J, Zhang D. Immobilizing Ni nanoparticles to mesoporous silica with size and location control via a polyol-assisted route for coking- and sintering-resistant dry reforming of methane. Chem Commun. 2014;50(55):7250.

28. Ding C, Wang J, Ai G, Liu S, Liu P, Zhang K, et al. Partial oxidation of methane over silica supported Ni nanoparticles with size control by alkanol solvent. Fuel. 2016;175:1–12.

29. Yu C, Hu J, Zhou W, Fan Q. Novel Ni/CeO_2-Al_2O_3 composite catalysts synthesized by one-step citric acid complex and their performance in catalytic partial oxidation of methane. J Energy Chem. 2014;23(2):235–43.

30. Ibrahim HH, Idem RO. Kinetic studies of the partial oxidation of gasoline (POXG) over a Ni– catalyst in a fixed-bed flow reactor. Chem Eng Sci. 2007;62(23):6582–

94.

31. Li H, Xu H, Wang J. Methane reforming with CO_2 to syngas over CeO_2-promoted Ni/Al2O_3-ZrO_2 catalysts prepared via a direct sol-gel process. J Nat Gas Chem. 2011;20(1):1–8.

32. Cheng Z, Wu Q, Li J, Zhu Q. Effects of Promoters and Preparation Procedures on Reforming of Methane with Carbon Dioxide over Ni/Al_2O_3 Catalyst. Catal Today. 1996;30(1–3):147–55.

33. Hartmann M, Maier L, Minh HD, Deutschmann O. Catalytic partial oxidation of iso-octane over rhodium catalysts: An experimental, modeling, and simulation study. Combust Flame. 2010;157(9):1771–82.

34. Hartmann M, Maier L, Deutschmann O. Hydrogen production by catalytic partial oxidation of iso-octane at varying flow rate and fuel/oxygen ratio: From detailed kinetics to reactor behavior. Appl Catal A Gen. 2011;391(1–2):144–52.

35. Li L, He S, Song Y, Zhao J, Ji W, Au CT. Fine-tunable Ni@porous silica core-shell nanocatalysts: Synthesis, characterization, and catalytic properties in partial oxidation of methane to syngas. J Catal. 2012;288:54–64.

36. Miao, Jianying, Ning Wang and PS. Methods for producing carbon nanostructures." U.S. Patent , issued September 14, 2010. 2010. p. 7,794,684.

37. Philip MR, Narayanan TN, Praveen Kumar M, Arya SB, Pattanayak DK. Self-protected nickel–graphene hybrid low density 3D scaffolds. J Mater Chem A. 2014;2(45):19488–94.

38. Zhang Y, Liu Y, Yang G, Endo Y, Tsubaki N. The solvent effects during preparation of Fischer-Tropsch synthesis catalysts: Improvement of reducibility, dispersion of supported cobalt and stability of catalyst. Catal Today. 2009;142(1–2):85–9.

39. Ming H, Baker BG. Characterization of cobalt Fischer-Tropsch catalysts I. Unpromoted cobalt-silica gel catalysts. Appl Catal A, Gen. 1995;123(1):23–36.

40. Sun S, Tsubaki N, Fujimoto K. The reaction performances and characterization of Fischer–Tropsch synthesis Co/SiO_2 catalysts prepared from mixed cobalt salts. Appl Catal A Gen. 2000;202(1):121–31.

41. Ho SW, Su YS. Effects of ethanol impregnation on the properties of silica-supported cobalt catalysts. J Catal. 1997;168(1):51–9.

42. Tao M, Meng X, Lv Y, Bian Z, Xin Z. Effect of impregnation solvent on Ni dispersion and catalytic properties of Ni/SBA-15 for CO methanation reaction. Fuel. 2016;165:289–97.

43. van Steen E, Sewell GS, Makhothe R a., Micklethwaite C, Manstein H, de Lange M, et al. TPR Study on the Preparation of Impregnated Co/SiO_2 Catalysts. J Catal. 1996;229(162):220–9.

44. Lucredio AF, Bellido JDA, Zawadzki A, Assaf EM. Co catalysts supported on SiO2 and γ-Al_2O_3 applied to ethanol steam reforming: Effect of the solvent used in the catalyst preparation method. Fuel. 2011;90(4):1424–30.

45. Dai, Y.M., Lu, C.Y. and Chang CJ. Catalytic activity of mesoporous Ni/CNT, Ni/SBA-15 and (Cu, Ca, Mg, Mn, Co)–Ni/SBA-15 catalysts for CO_2 reforming of CH 4. RSC Adv. 2016;6(77):73887–96.

46. Coq B, Figueras F. Bimetallic palladium catalysts: Influence of the co-metal on the catalyst performance. J Mol Catal A Chem. 2001;173(1–2):117–34.

47. Liu Z, Zhou J, Cao K, Yang W, Gao H, Wang Y, et al. Highly dispersed nickel loaded on mesoporous silica: One-spot synthesis strategy and high performance as catalysts for methane reforming with carbon dioxide. Appl Catal B Environ. 2012;125:324–30.

48. Baker RTK, Barber MA, Harris PS, Feates FS, Waite RJ. Nucleation and growth of carbon deposits from the nickel catalyzed decomposition of acetylene. J Catal. 1972;26(1):51–62.

49. Fatsikostas AN, Verykios XE. Reaction network of steam reforming of ethanol over Ni-based catalysts. J Catal. 2004;225(2):439–52.

50. Arslan A, Gunduz S, Dogu T. Steam reforming of ethanol with zirconia incorporated mesoporous silicate supported catalysts. Int J Hydrogen Energy. 2014;39(32):18264–72.

51. Carrera Cerritos R, Fuentes Ramírez R, Aguilera Alvarado AF, Martínez Rosales JM, Viveros García T, Galindo Esquivel IR. Steam Reforming of Ethanol over Ni/Al2O3−La2O3 Catalysts Synthesized by Sol−Gel. Ind Eng Chem Res. 2011;50(5):2576–84.

52. Van Santen RA. Complementary structure sensitive and insensitive catalytic relationships. Acc Chem Res. 2009;42(1):57–66.

53. Bengaard HS, Nørskov JK, Sehested J, Clausen BS, Nielsen LP, Molenbroek AM, et al. Steam Reforming and Graphite Formation on Ni Catalysts. J Catal. 2002;209(2):365–84.

54. Christensen KO, Chen D, Lødeng R, Holmen A. Effect of supports and Ni crystal size on carbon formation and sintering during steam methane reforming. Appl Catal A Gen. 2006;314(1):9–22.

55. Kim J-H, Suh DJ, Park T-J, Kim K-L. Effect of metal particle size on coking during CO_2 reforming of CH_4 over Ni–alumina aerogel catalysts. Appl Catal A Gen. 2000;197(2):191–200.

56. Tang S, Ji L, Lin J, Zeng HC, Tan KL, Li K. CO_2 Reforming of Methane to Synthesis Gas over Sol–Gel-made Ni/γ-Al_2O_3 Catalysts from Organometallic Precursors. J Catal. 2000;194(2):424–30.

57. Zhang, J., Wang, H. and Dalai AK. Effects of metal content on activity and stability of Ni-Co bimetallic catalysts for CO_2 reforming of CH_4. Appl Catal A Gen. 2008;339(2):121–9.

58. Borowiecki T. Nickel catalysts for steam reforming of hydrocarbons: phase composition and resistance to coking. Appl Catal. 1984;10(3):273–89.

59. Wan H, Li X, Ji S, Huang B, Wang K, Li C. Effect of Ni Loading and CexZri-xO_2

Promoter on Ni-Based SBA-15 Catalysts for Steam Reforming of Methane. J Nat Gas Chem. 2007;16(2):139–47.

60. Liu Q, Gao J, Zhang M, Li H, Gu F, Xu G, et al. Highly active and stable Ni/γ-Al_2O_3 catalysts selectively deposited with CeO_2 for CO methanation. RSC Adv. 2014;4(31):16094.

61. Damyanova S, Pawelec B, Arishtirova K, Fierro JLG. Ni-based catalysts for reforming of methane with CO2. Int J Hydrogen Energy. 2012;37(21):15966–75.

62. Du X, Zhang D, Shi L, Gao R, Zhang J. Coke- and sintering-resistant monolithic catalysts derived from in situ supported hydrotalcite-like films on Al wires for dry reforming of methane. Nanoscale. 2013;5(7):2659–63.

63. Sugisawa M, Takanabe K, Harada M, Kubota J, Domen K. Effects of la addition to Ni/Al_2O_3 catalysts on rates and carbon deposition during steam reforming of n-dodecane. Fuel Process Technol. 2011;92(1):21–5.

64. Soykal II, Sohn H, Singh D, Miller JT, Ozkan US. Reduction characteristics of ceria under ethanol steam reforming conditions: Effect of the particle size. ACS Catal. 2014;4(2):585–92.

65. Nikolla E, Holewinski A, Schwank J, Linic S. Controlling carbon surface chemistry by alloying: Carbon tolerant reforming catalyst. J Am Chem Soc. 2006;128(35):11354–5.

66. Nikolla E, Schwank J, Linic S. Promotion of the long-term stability of reforming Ni catalysts by surface alloying. J Catal. 2007;250(1):85–93.

67. Nikolla E, Schwank JW, Linic S. Hydrocarbon steam reforming on Ni alloys at solid oxide fuel cell operating conditions. Catal Today. 2008;136(3–4):243–8.

68. Guo Y, Li H, Jia L, Kameyama H. Trace Ru-doped anodic alumina-supported Ni catalysts for steam reforming of kerosene: Activity performance and electrical-heating possibility. Fuel Process Technol. 2011;92(12):2341–7.

69. Ibrahim HH, Kumar P, Idem RO. Reforming of isooctane over Ni-Al_2O_3 catalysts

for hydrogen production: Effects of catalyst preparation method and nickel loading. Energy and Fuels. 2007;21(2):570–80.

70. Prieto G, Zečević J, Friedrich H, de Jong KP, de Jongh PE. Towards stable catalysts by controlling collective properties of supported metal nanoparticles. Nat Mater. 2012;12(1):34–9.

71. Xiao, Zhourong, Chan Wu, Ling Li, Guozhu Li, Guozhu Liu and LW. Pursuing complete and stable steam reforming of n-dodecane over nickel catalysts at low temperature and high LHSV. Int J Hydrogen Energy. 2017;42(8):5606–18.

FIGURE CAPTIONS

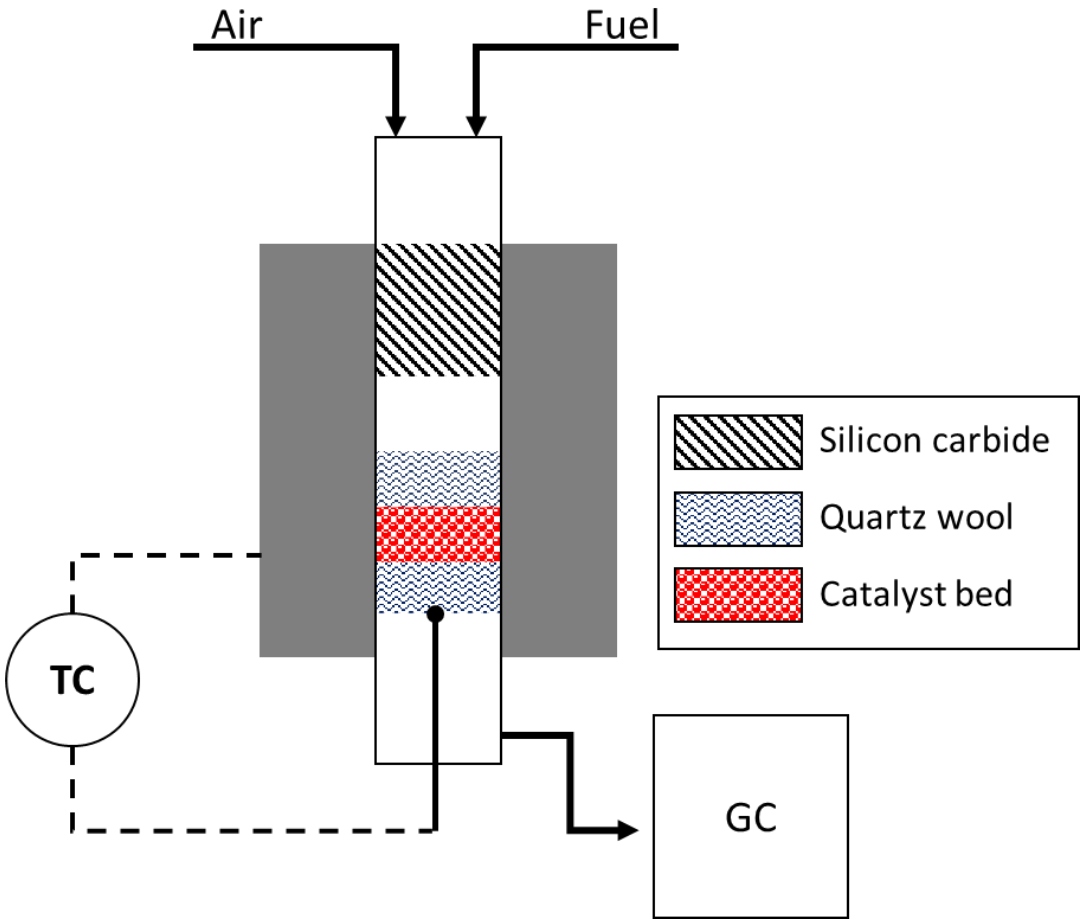

Figure 1. Diagram of experimental setup for partial oxidation .

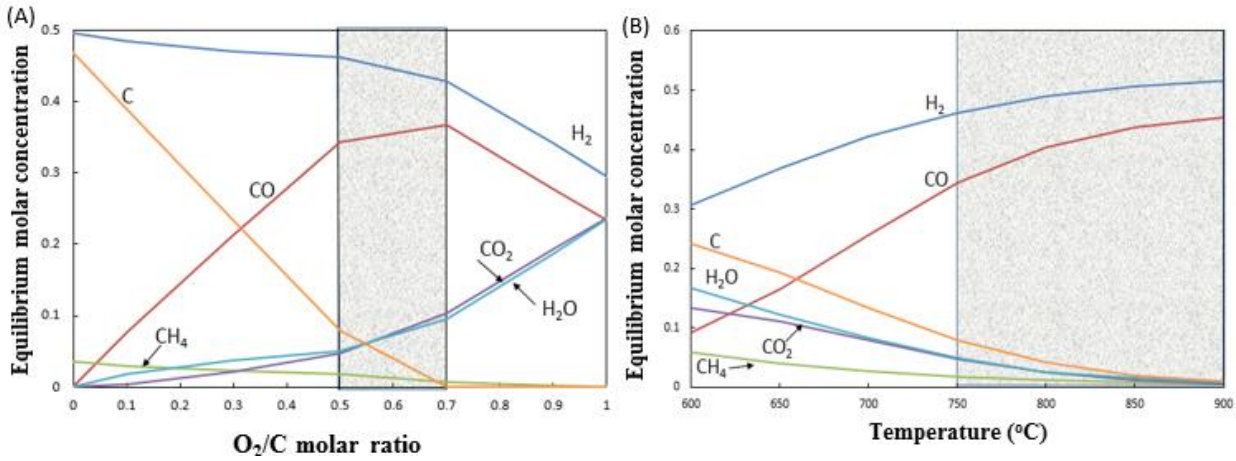

Figure 2. Thermodynamic analysis of the partial oxidation of isooctane at atmospheric pressure: (A) the effect of O_2/C ratio at a fixed temperature of 750 ^oC and (B) the effect of temperature at a fixed O_2/C ratio of 0.5 on the molar concentrations of gas (Gray area represents the operation conditions that may lower the carbon formation with high syngas production)

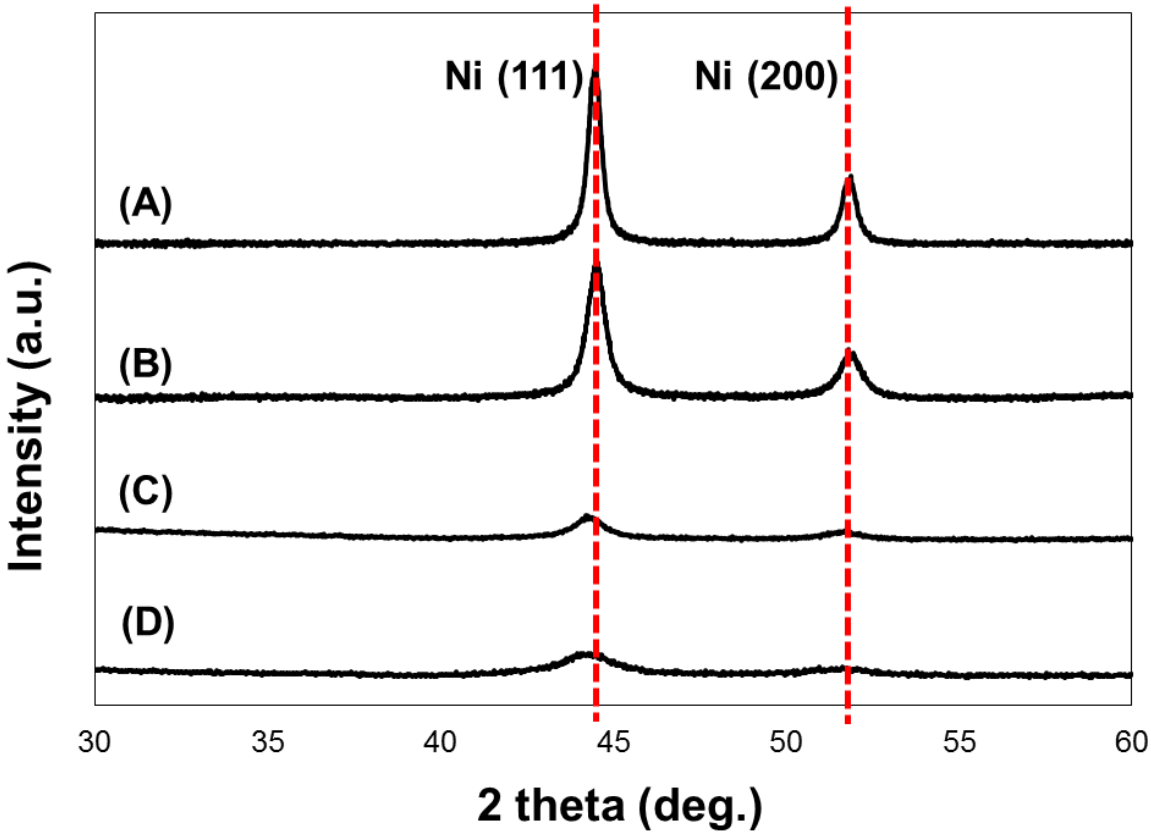

Figure 3. XRD patterns of NS-W700 (A), NS-W500 ((B), NS-EG (C), and NCS-EG (D). The sample nomenclatures are explained in Table 1.

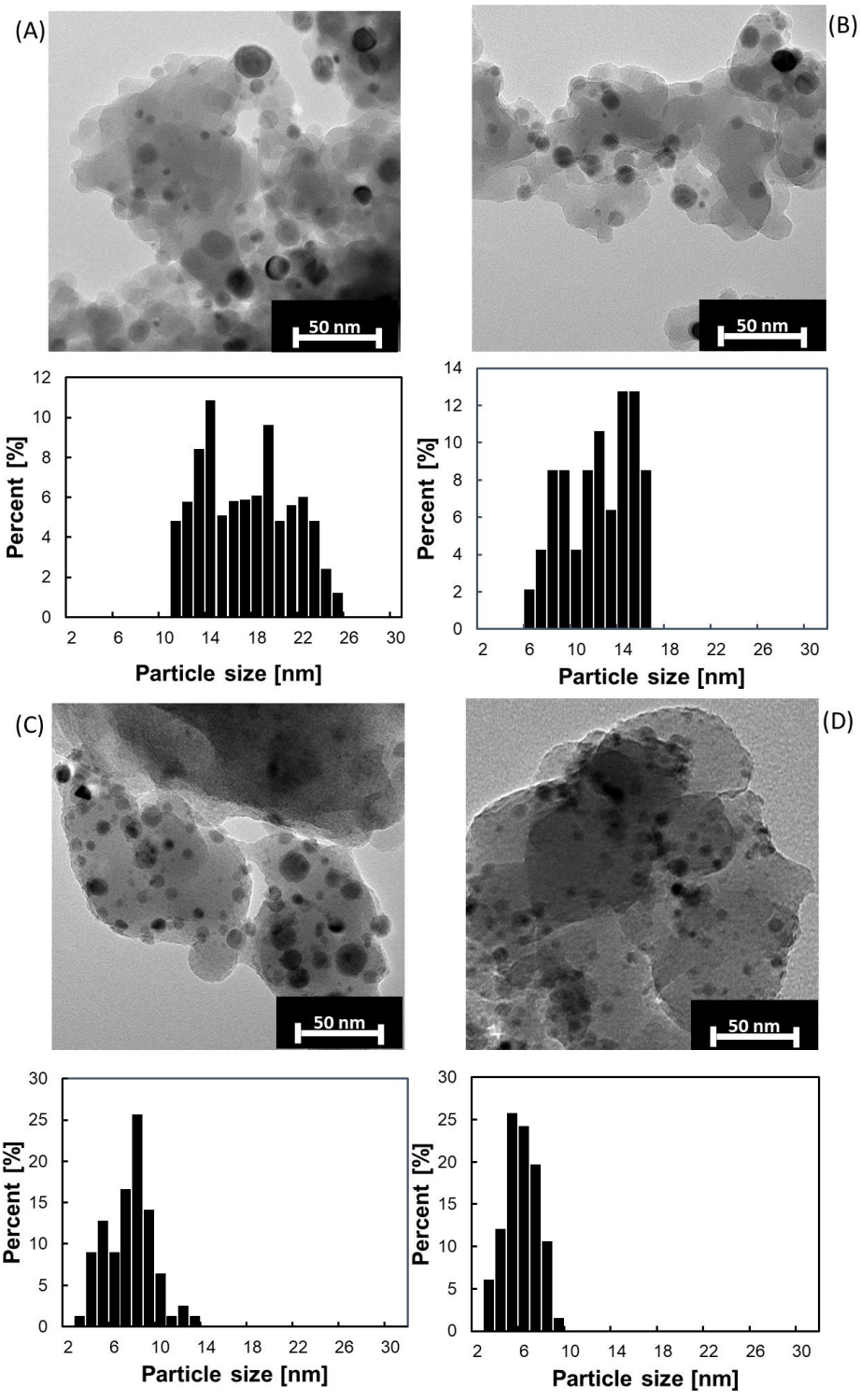

Figure 4. TEM images of NS-W700 (A), NS-W500 (B), NS-EG (C), and NCS-EG (D) with the size distribution of Ni NPs

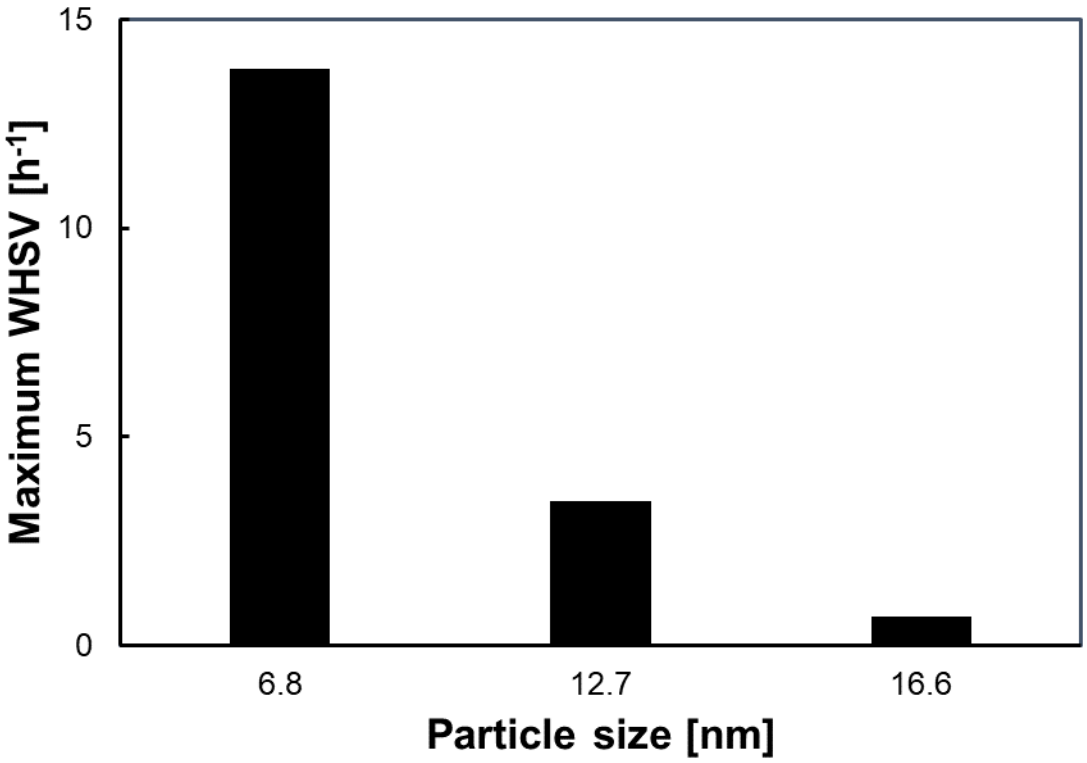

Figure 5. The effect of Ni particle sizes on maximum working WHSV (Maximum WHSV is determined by the catalyst deactivation due to the severe carbon formation).

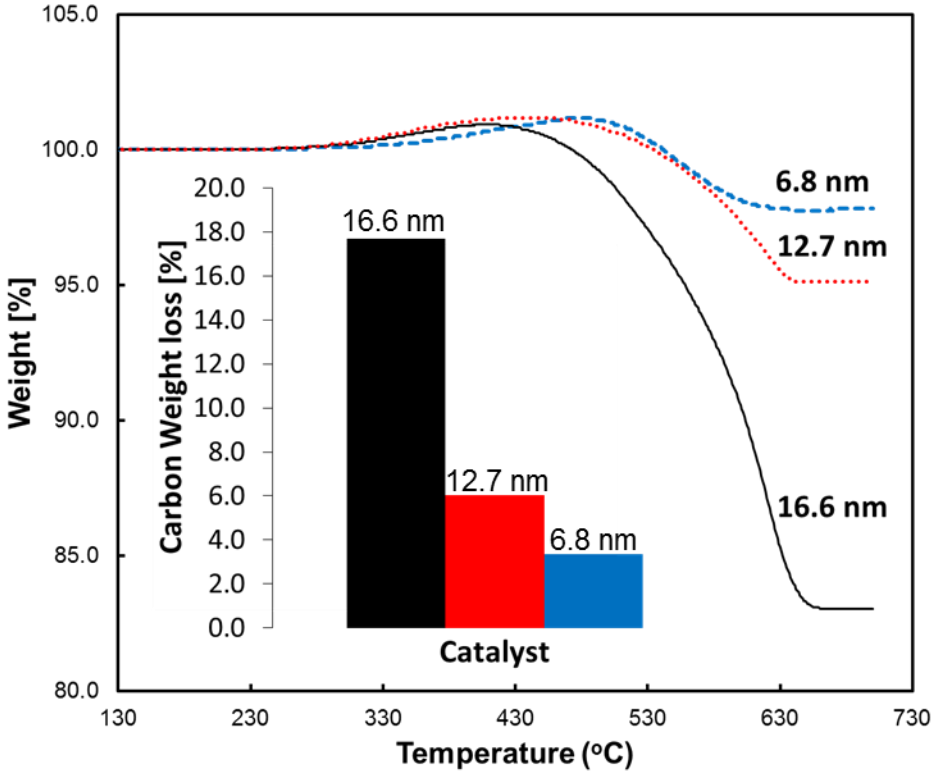

Figure 6. TGA profiles after 2 h of fuel reforming test (750 °C, WHSV of 13.8 h^{-1}, mass of catalyst of 0.1, and O_2/C=0.5. Isooctane, N_2 and air flow rates were 2 ml/h, 50 sccm, and 125 sccm, respectively).

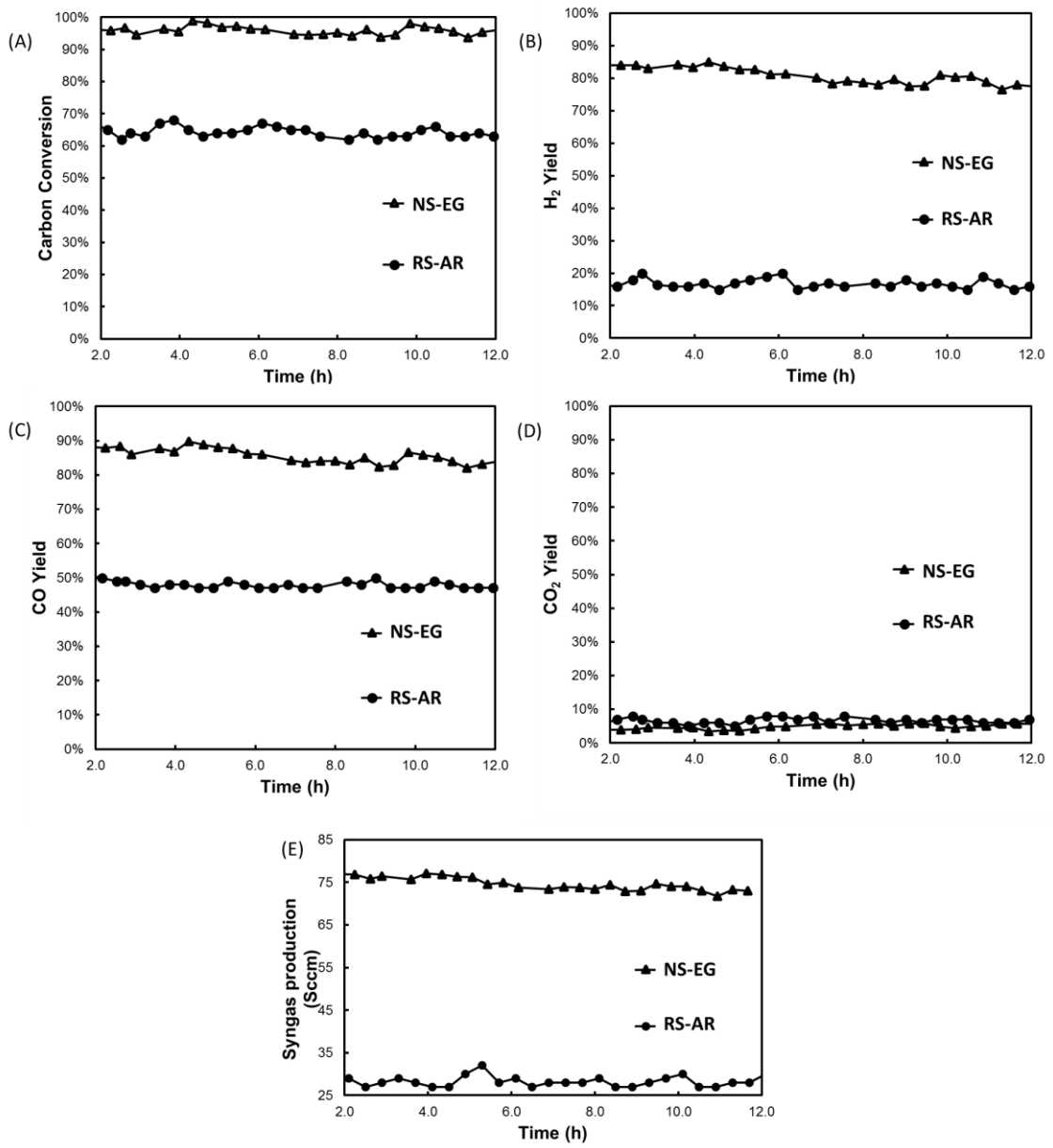

Figure 7. Isooctane conversion (A), H_2 yield (B), CO yield (C), CO_2 yield (D), and synthesis gas production (E) of the NS-EG and RS-AR, respectively. The partial oxidation reactions were performed at 750 ^{o}C, WHSV of 13.8 h^{-1}, residence time of 35 ms, catalyst mass of 0.1, and O_2/C=0.5. The flow rates of isooctane, N_2 and air were fixed at 2 ml/h, 50 sccm, and 86 sccm, respectively.

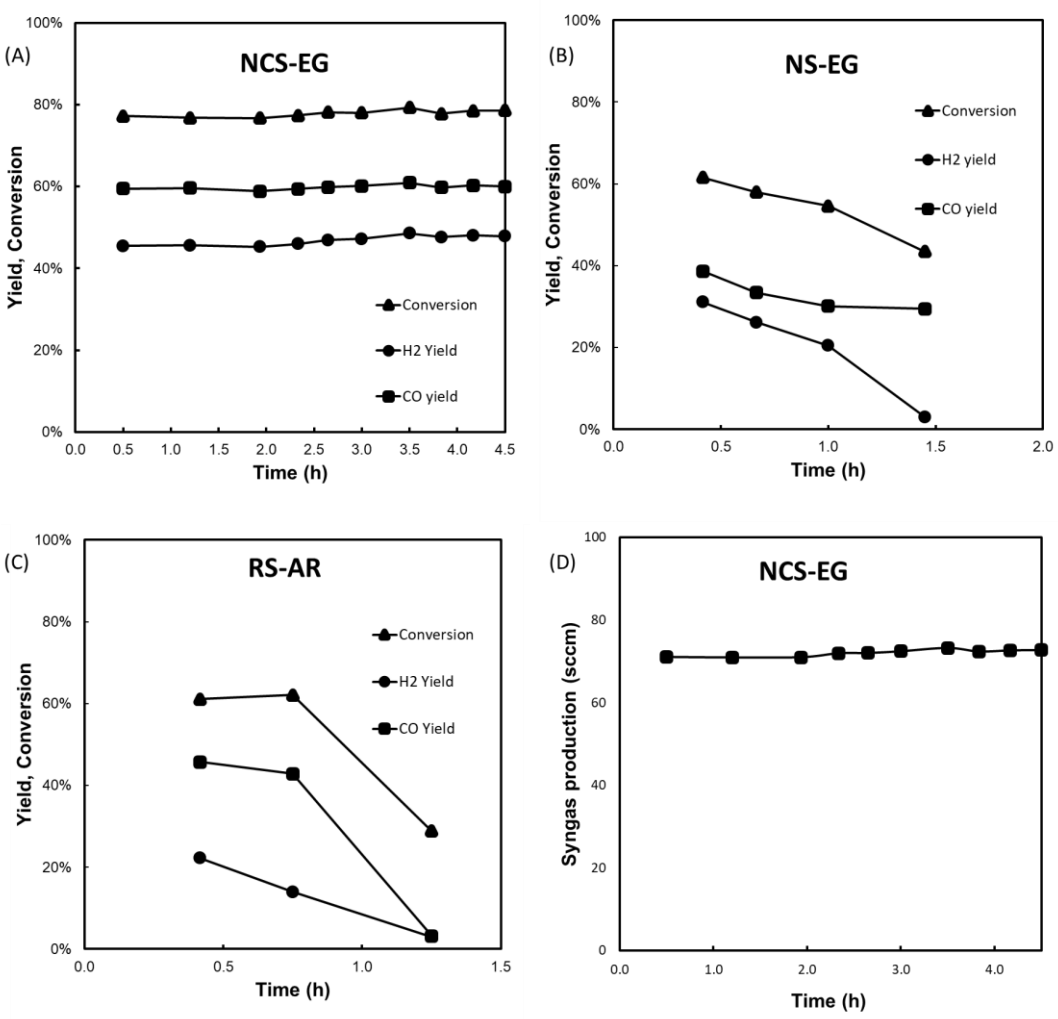

Figure 8. Isooctane conversion, H_2 yield and CO yield of NCS-EG (A) NS-EG (B) and RS-AR (C) and synthesis gas production of the NCS-EG (D), at the accelerated conditions (750 ^{o}C, WHSV of 20.01 h^{-1}, residence time of 23 ms, mass of catalyst of 0.1, O_2/C=0.5 and isooctane, N_2 and air flow rates of 2.9 ml/h, 50 sccm, and 125 sccm respectively).

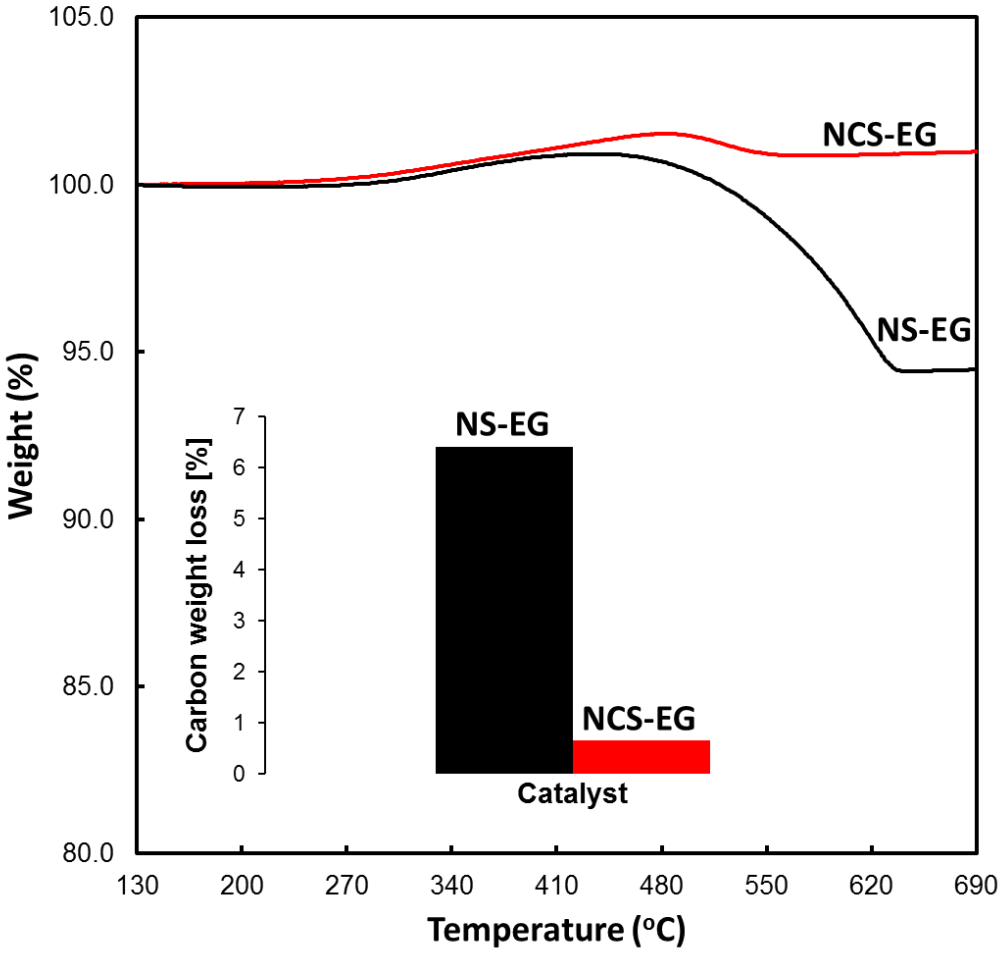

Figure 9. TGA profiles of NCS-EG and NS-EG after the accelerated conditions activity tests at WHSV of 20.01 h^{-1}. residence time of 23 ms, catalyst mass of 0.1, O_2/C=0.5, and isooctane, N_2 and air flow rates of 2.9 ml/h, 50 sccm, and 125 sccm, respectively.

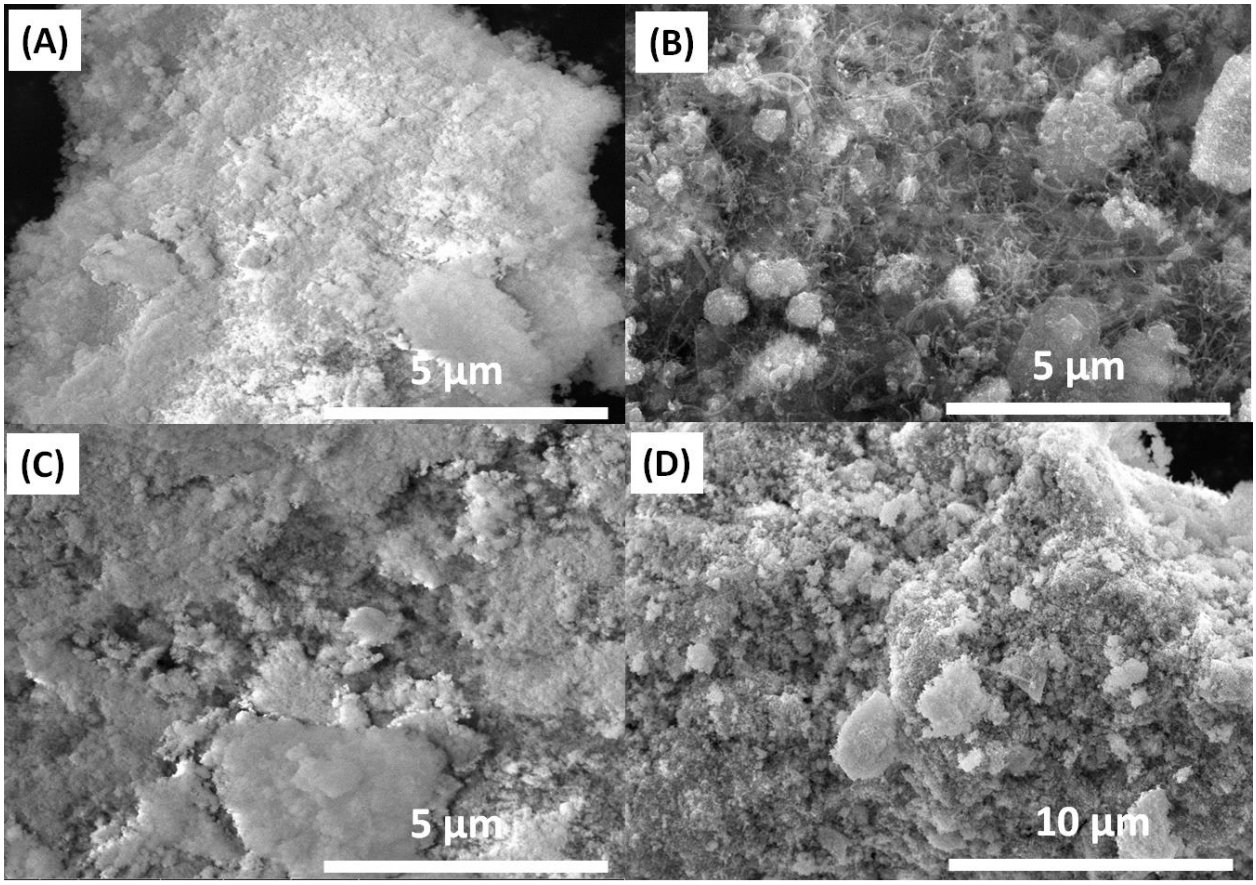

Figure 10. SEM images of fresh NS-EG (A) and NCS-EG (C), and spend NS-EG (B) and NCS-EG (D) after activity tests at accelerated conditions (WHSV of 20.01 h^{-1}, residence time of 23 ms, catalyst mass of 0.1, and O_2/C=0.5) Isooctane, N_2 and air flow rates were 2.9 ml/h, 50 sccm, and 125 sccm, respectively.

Table 1. Catalyst Composition

Sample	Ni wt.%	Ce wt.%	Rh wt.%	Solvent[1]	Calcination Temperature (^oC)
NS-W500[2]	11	0	0	W	500
NS-W700[3]	11	0	0	W	700
NS-EG[4]	11	0	0	EG	700
NCS-EG[5]	11	3	0	EG	700
RS-AR[6]	0	0	1	AR	700

[1]W: water, EG: ethylene glycol, AR: aqua regia

[2]NS-W500 = Ni/SiO_2 using water solvent and calcination temperature of 500^{o}C.

[3]NS-W700 = Ni/SiO_2 using water solvent and calcination temperature of 700^{o}C.

[4]NS-EG = Ni/SiO_2 using EG solvent and calcination temperature of 700^{o}C.

[5]NCS-EG = $NiCe/SiO_2$ using EG solvent and calcination temperature of 700^{o}C.

[6]RS-AR = Rh/SiO_2 using calcination temperature of 700^{o}C

Table 2. Reactions possible during Partial Oxidation of Isooctane.

Reaction	Equation	ΔH_{298K} (kJ/mol)
Partial oxidation (POX)	$i\text{-}C_8H_{18} + 4O_2 \rightleftarrows 8CO + 9H_2$	-659.9
Steam reforming (SR)	$i\text{-}C_8H_{18} + 8H_2O \rightleftarrows 8CO + 17H_2$	1261
Dry reforming (DR)	$i\text{-}C_8H_{18} + 8CO_2 \rightleftarrows 16CO + 9H_2$	1590
Water gas shift (WGS)	$CO + H_2O \rightleftarrows CO_2 + H_2$	-41
Complete oxidation (COX)	$i\text{-}C_8H_{18} + 12.5O_2 \rightleftarrows 8CO_2 + 9H_2O$	-5457
Methanation	$CO + 3H_2 \rightleftarrows CH_4 + H_2O$	-206
Boudouard reaction	$2CO \rightleftarrows CO_2 + C$	-172

Table 3. Average Crystallite sizes for fresh catalyst samples

Catalyst	XRD average crystallite size [nm]	TEM average particle size [nm]
NS-W700	21.6	16.6 ± 1.8
NS-W500	14.8	12.7± 2.5
NS-EG	5.7	6.8± 2.1
NCS-EG	3.8	5.2± 1.4
RS-AR	X*	2.8± 0.9

*Rh particle size could not be detected in the XRD.